Supporting information

Single-Atom Tungsten Doped $Nis_{0.5}Se_{0.5}$ Nanosheets@Nanorods Heterostructures Catalyze Water Splitting Highly Active and Durable

Experimental Section

Selenium powder (Se, 99.999%), thiourea (CN_2H_4S, 99.0%), tungsten trioxide (WO_3, 98%), hydrazine hydrate ($N_2H_4 \cdot H_2O$, 80%), ammonium fluoride (NH_4F, 98.0%), Nickel sulfide (NiS, 99.9%), Nickel selenide (NiSe, 99.9%), tungsten Sulfide (WS_2, 99.9%), tungsten Selenide (WSe_2, 99.9%), Potassium hydroxide (KOH, 90%) and 5 wt.% Nafion solution were all purchased from Adamas Chemical Reagent Co. Ltd. Ethanol (CH_3CH_2OH, ≥ 99.8%), acetone (CH_3COCH_3, ≥ 99.5%), and isopropyl alcohol (C_3H_8O, ≥ 99.8%), hydrochloric acid (HCl, 37%) were purchased from Kermel (Tianjin, China). All chemicals were used as received without further purification. The deionized (DI) water was produced by an ultrapure water system (Millipore).

***Synthesis of W-NiS*.**

To synthesize W-NiS, the same condition as mentioned above except no selenium powder in the W-$NiS_{0.5}Se_{0.5}$ prepared process.

***Synthesis of W-NiSe*.**

To synthesize W-NiSe, the same condition as mentioned above except no thiourea powder in the W-$NiS_{0.5}Se_{0.5}$ prepared process.

***Synthesis of $NiS_{0.5}Se_{0.5}$*.**

In a typical synthesis of the $NiS_{0.5}Se_{0.5}$, to remove the nickel oxides on the NF surface, the NF was soaked in 1 M HCl solution firstly, then washed with DI water, acetone and ethanol in turns. The NF was dried in a vacuum oven to avoid reoxidation. In detail, 0.288 g selenium powder was firstly dissolved in 6 ml hydrazine hydrate and then added 0.278 g thiourea and 0.4 g ammonium fluoride. At last, 15 ml ethanol and 9 ml water were added. After stirring for 0.5 h, the obtained solution with a dried NF (1 x 2.5 cm^2) was put into a 50 ml Teflon-lined stainless autoclave to process the solvothermal reaction at 200 °C for 20 h. After cooling to the room temperature, the obtained $NiS_{0.5}Se_{0.5}$ nanorod@nanosheet hybrid ($NiS_{0.5}Se_{0.5}$) was washed with DI water for three times then frozen drying. To convert the above sample to the corresponding NiS_xSe_{1-x}, changing the relevant S: Se molar ratio[1].

***Synthesis of NiS*.**

To synthesize NiS, the same condition as mentioned above except no selenium powder in the $NiS_{0.5}Se_{0.5}$ prepared process.

***Synthesis of NiSe*.**

To synthesize NiSe, the same condition as mentioned above except no thiourea powder in the $NiS_{0.5}Se_{0.5}$ prepared process.

Calculation of e_g filling.

The temperature-dependent magnetizations (M-T) for the prepared samples were performed under H = 1 kOe. The total effective magnetic moment (μ_{eff}) can be obtained by $\mu_{eff} = \sqrt{8C}\,\mu_B$ through χ^{-1}–T liner fitting result, in which C is Curie constant and obtained from the magnetizations (χ = M/H) above 150 K according to Curie–Weiss law[2].

For Ni ions, μ_{eff} can also be calculated from the relationship[3]:

$$\mu_{eff} = g\mu_B\sqrt{S_{LS}(S_{LS}+1)V_{LS} + S_r(S_{HS}+1)V_{HS}}$$

where g is g factor, S_{LS}(=0) and S_{HS}(=2) are the S value, and V_{LS} and V_{HS}(=1-V_{LS}) are the volume fractions for Ni^{2+} ions. Therefore, using above two values, the e_g electron (x) can be further calculated by $x = S_{LS} * V_{LS} + S_{HS} * V_{HS}$.

Calculation of turnover frequencies (TOFs)

The TOFs per metal site were calculated according to the hypothesis that all metal atoms (W and Ni) of the nanomaterials served as active sites and contacted with the electrolyte. The following formula was applied to calculate the turnover frequency (TOFs) per active site in $NiS_{0.5}Se_{0.5}$[4]:

$$TOFs = \frac{\text{\# toal hydrogen turnover /cm}^2 \text{ geomrtric aera}}{\text{\# active sites /cm}^2 \text{ geomrtric aera}}$$

$$TOFs = \frac{\text{\# toal oxygen turnover /cm}^2 \text{ geomrtric aera}}{\text{\# active sites /cm}^2 \text{ geomrtric aera}}$$

In addition, the calculated TOFs for W-$NiS_{0.5}Se_{0.5}$ require another equation[5]:

$$TOFs_{\text{cal}} = TOFs_{Ni}X_{Ni} + TOFs_{W}(1 - X_{Ni})$$

$$X_{Ni} = \frac{\text{number of active Ni atoms (mol)}}{\text{total number of active Ni and W atoms (mol)}}$$

According to the above mentioned hypothesis, all the active sites were accessible to the electrolyte. Therefore, in the practical condition, it is needed to note that the number of practical active sites are considered to be lower than the theoretical value.

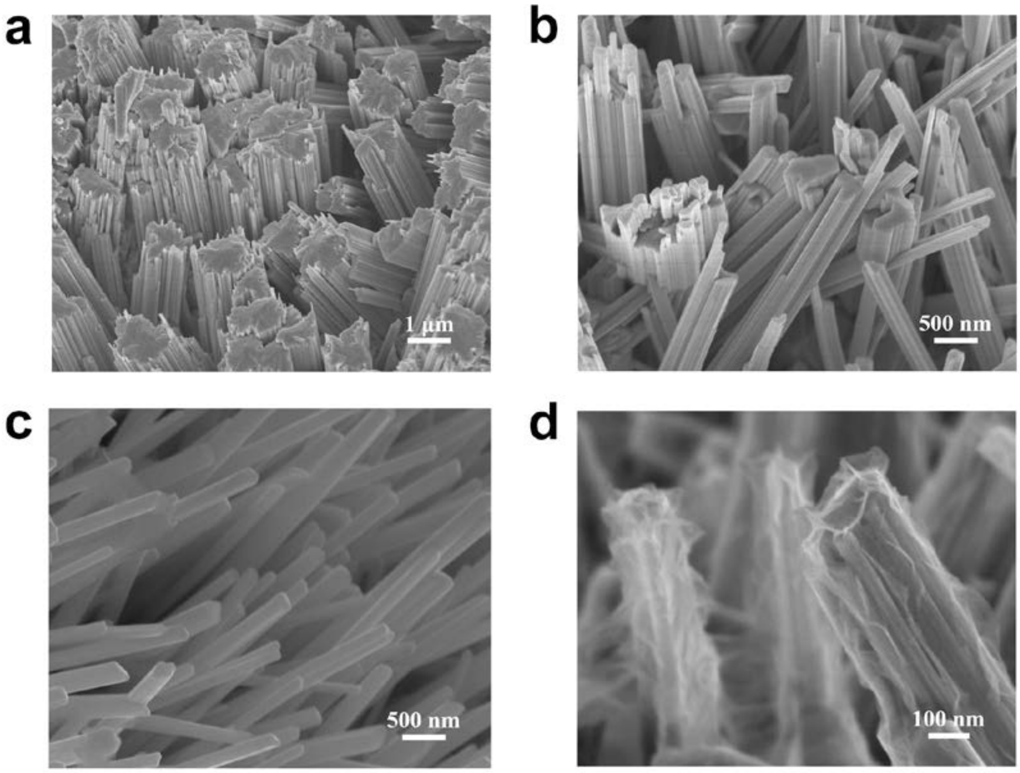

Supplementary Fig. 1 SEM images of the W-$NiS_{0.5}Se_{0.5}$ at the different stages of the hydrothermal process (a) 5 h; (b) 10 h; (c) 15 h and (d) 20 h.

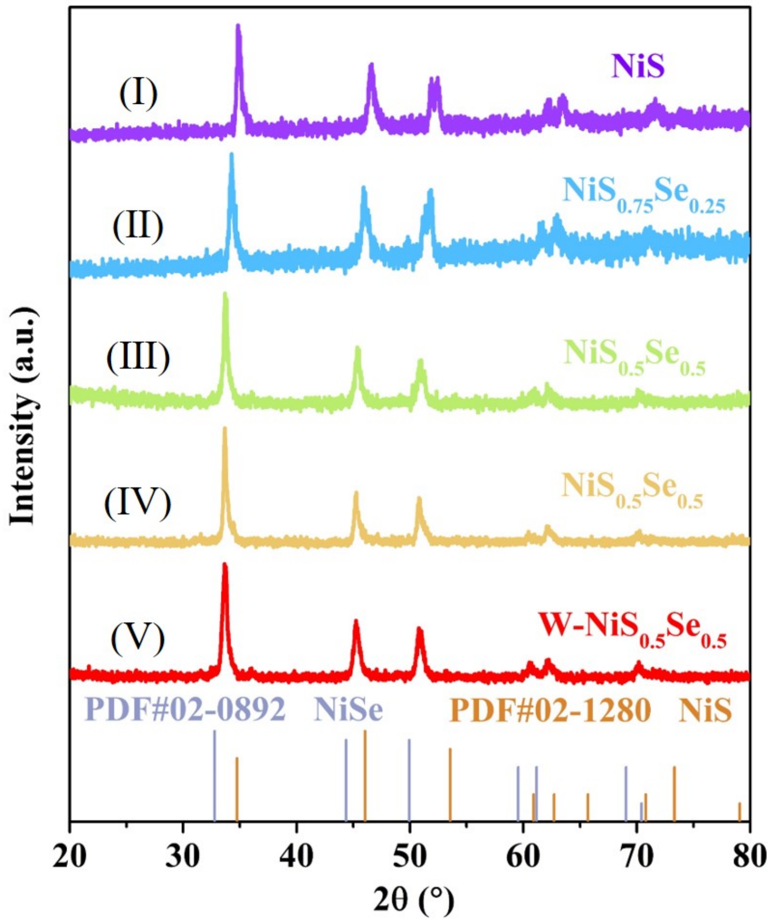

Supplementary Fig. 2 XRD patterns of the W-$NiS_{0.5}Se_{0.5}$ at different stages of the hydrothermal process (I) 5 h; (II) 10 h; (III) 15 h; (IV) 20 h; (V) 24 h.

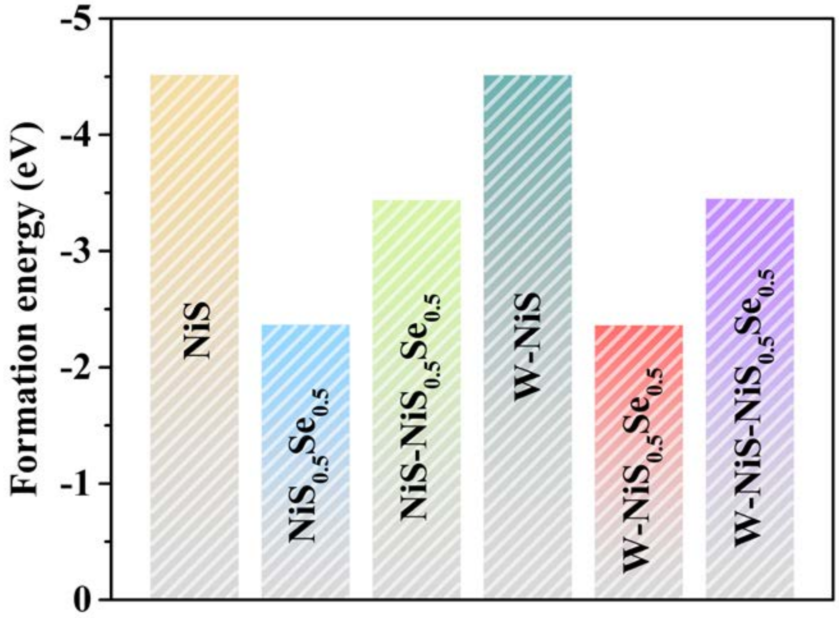

Supplementary Fig. 3 The formation energy of prepared samples.

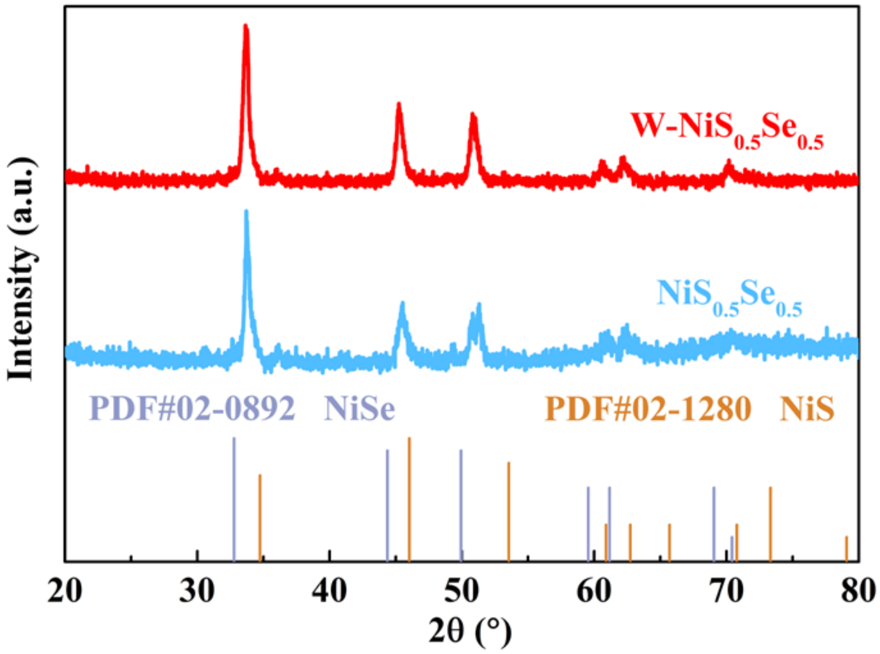

Supplementary Fig. 4 XRD patterns of W-$NiS_{0.5}Se_{0.5}$ and $NiS_{0.5}Se_{0.5}$.

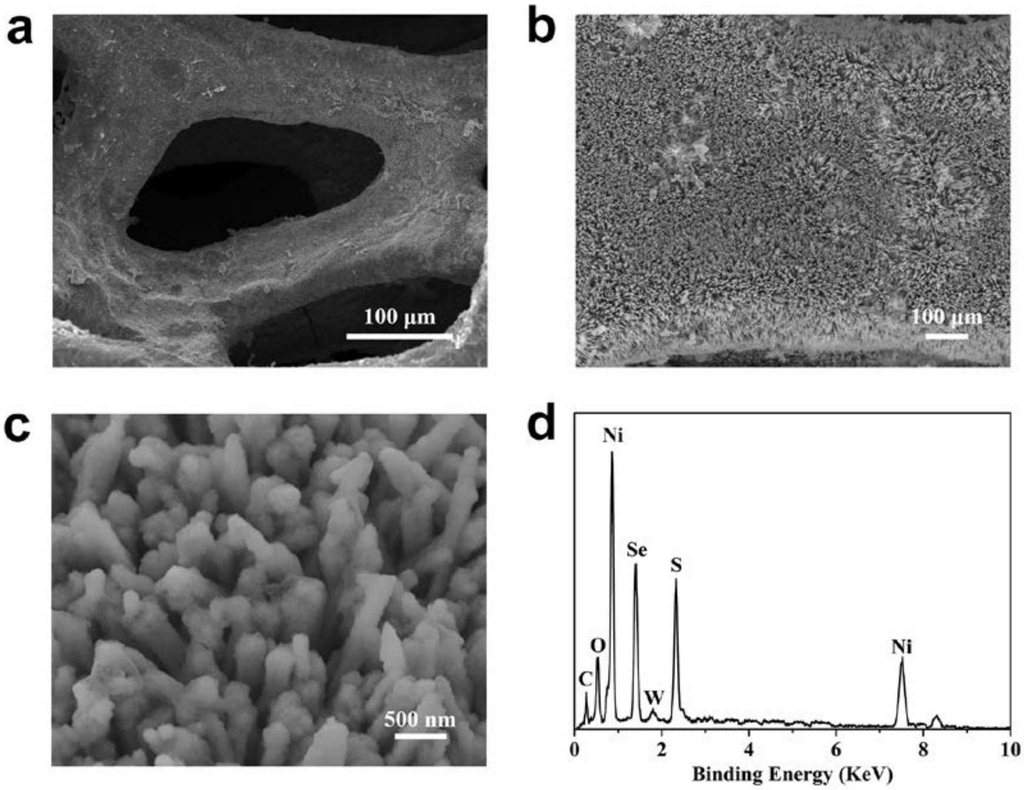

Supplementary Fig. 5 (a-c) SEM images at different magnifications; (d)EDX spectrum of the W-$NiS_{0.5}Se_{0.5}$.

From high magnification SEM, we can see that the nanorod is wrapped by nanosheets and the diameter locates about 260 nm. From low magnification SEM, it can be seen that the nanorods are uniform and evenly grown on nickel foam skeleton. The atomic ratio of W: Ni: S: Se was 1.73: 49.67: 24.28: 24.32 from EDX (Supplementary Table 1).

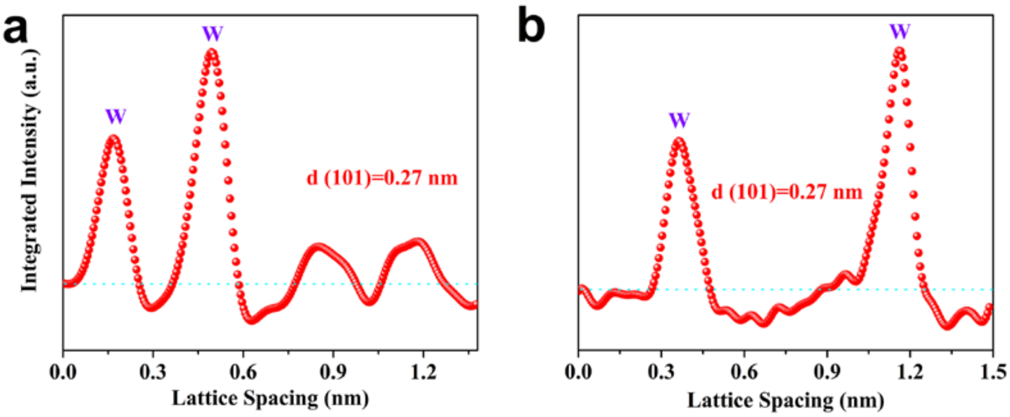

Supplementary Fig. 6 Line-scanning intensity profile obtained from the area highlighted with the yellow arrow in regions as shown in Fig. 1f.

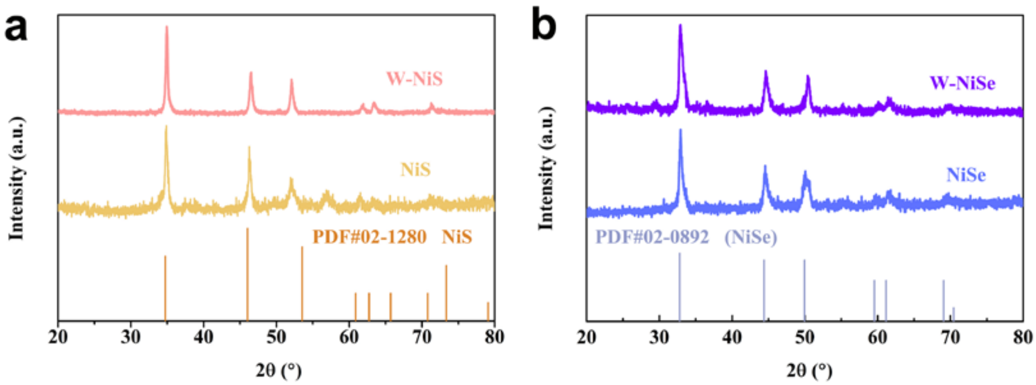

Supplementary Fig. 7 XRD patterns of (a) W-NiS and NiS; (b) W-NiSe and NiSe.

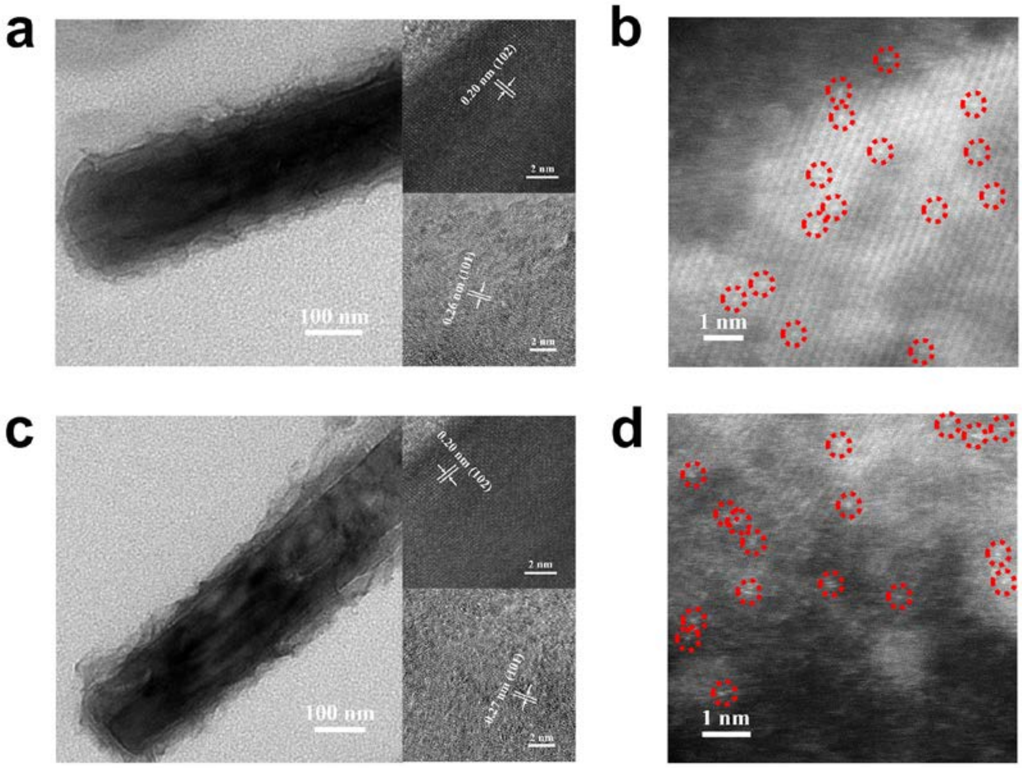

Supplementary Fig. 8 The TEM, HRTEM, HAADF-STEM image of the (a-b) W-NiS and (c-d) W-NiSe.

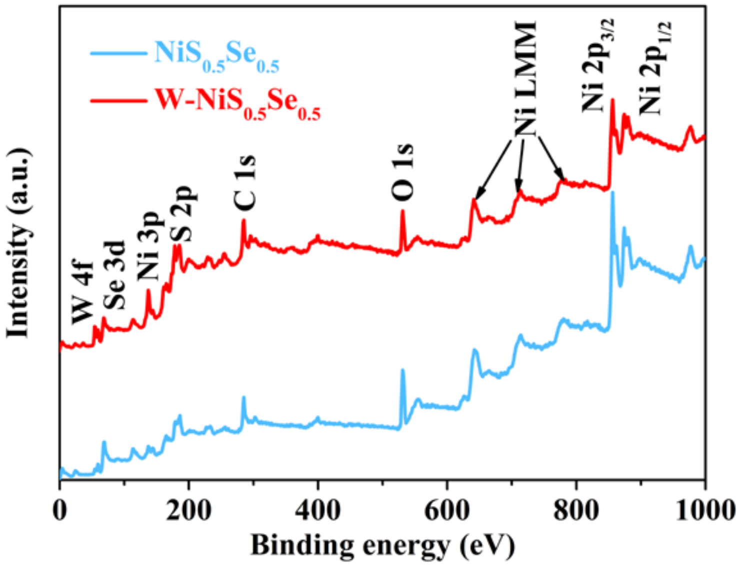

Supplementary Fig. 9 The XPS survey spectra of the W-$NiS_{0.5}Se_{0.5}$ and $NiS_{0.5}Se_{0.5}$.

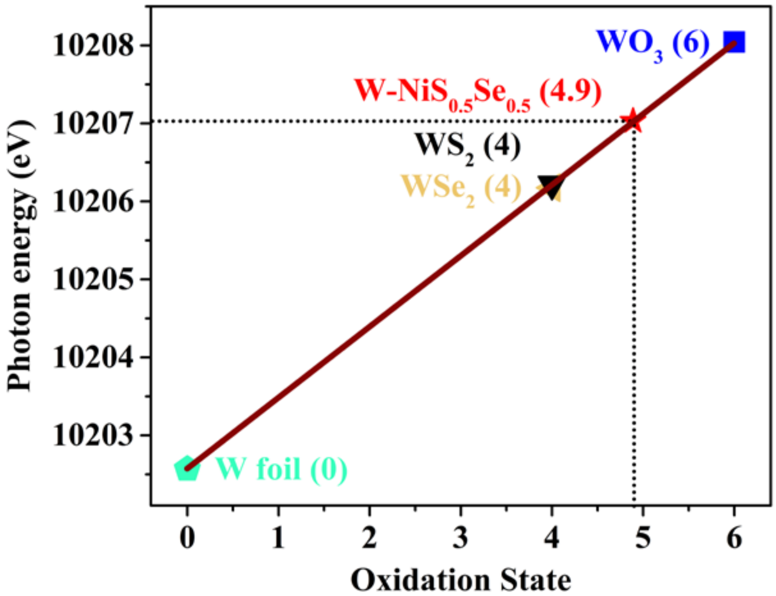

Supplementary Fig. 10 The calculated average oxidation state of W in W-$NiS_{0.5}Se_{0.5}$ from XAS.

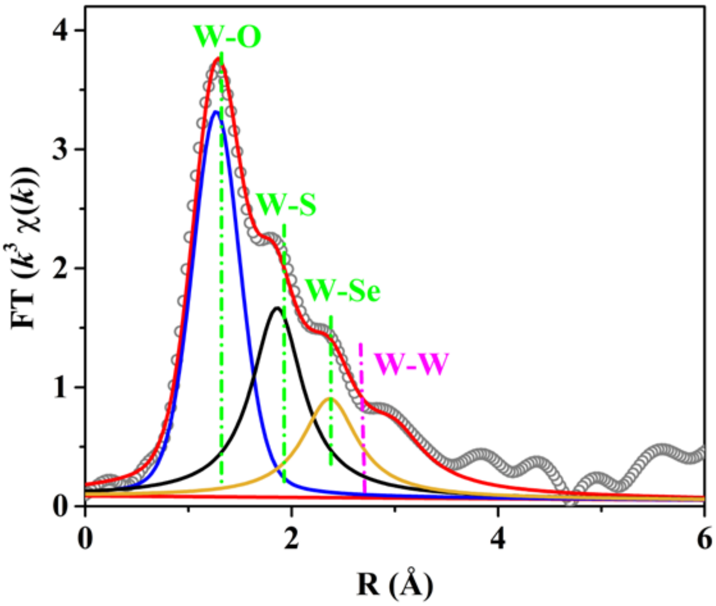

Supplementary Fig. 11 Fourier transformed EXAFS spectra of the W-$NiS_{0.5}Se_{0.5}$ at the W L_3-edge (scatter points) and the theoretical fits (solid lines).

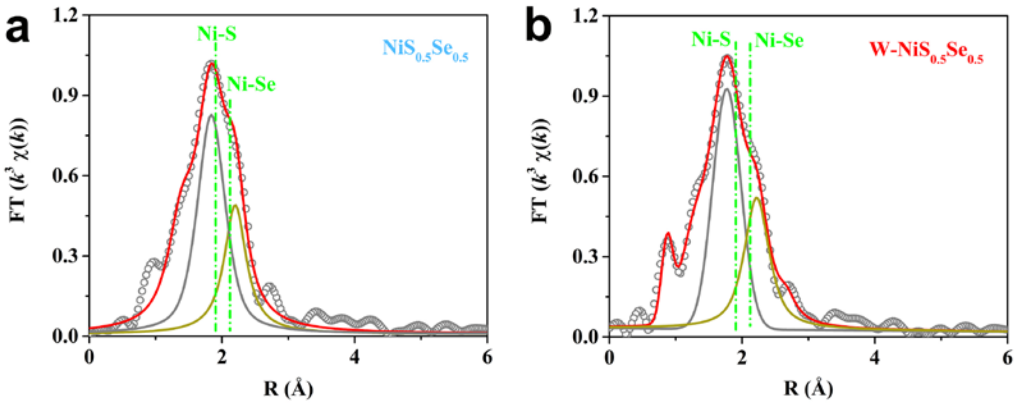

Supplementary Fig. 12 Fourier transformed EXAFS spectra of the (a) $NiS_{0.5}Se_{0.5}$ and (b) W-$NiS_{0.5}Se_{0.5}$ at the Ni K-edge (scatter points) and the theoretical fits (solid lines).

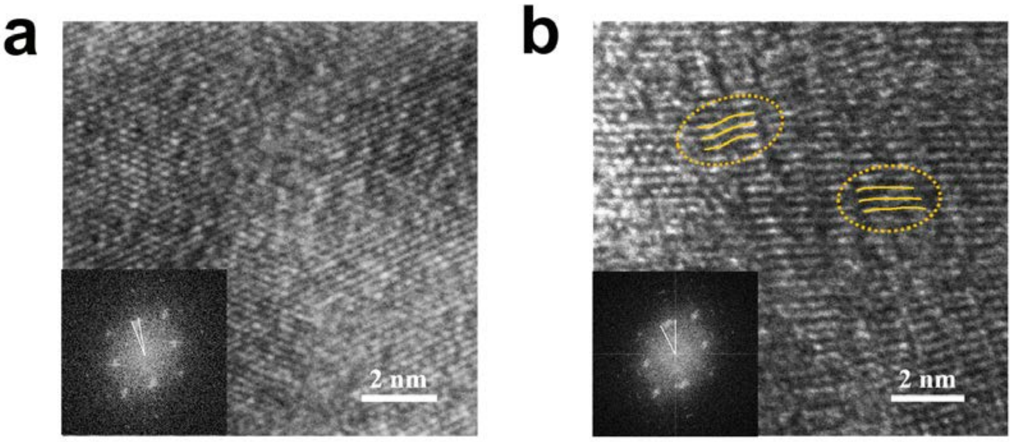

Supplementary Fig. 13 HRTEM images and corresponding FFT patterns (insets) for (a) virgin $NiS_{0.5}Se_{0.5}$ and (b) W-$NiS_{0.5}Se_{0.5}$. The subtle distortion regions are marked by the orange lines in the Supplementary Fig. 13b.

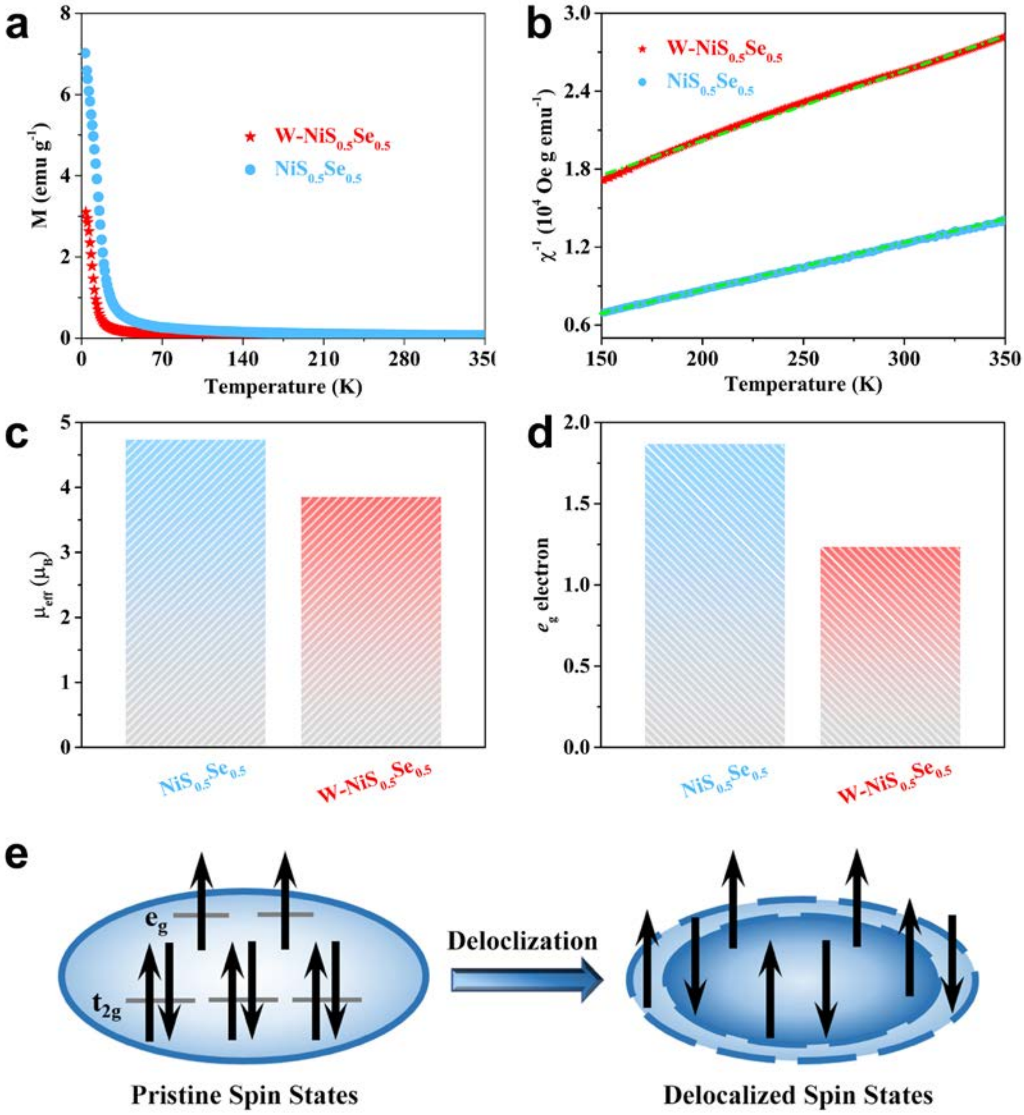

Supplementary Fig. 14 (a) Temperature dependent magnetization under H=1 kOe; (b) Temperature dependent inverse susceptibilities fitted by Curie–Weiss law, and calculated (c) effective magnetic moment (μ_{eff}) and (d) e_g occupancy of W-$NiS_{0.5}Se_{0.5}$ and $NiS_{0.5}Se_{0.5}$. (e) Schematic representations of the formation mechanism for the subtle distortion of atomic arrangement through the incorporated heterogeneous spin states.

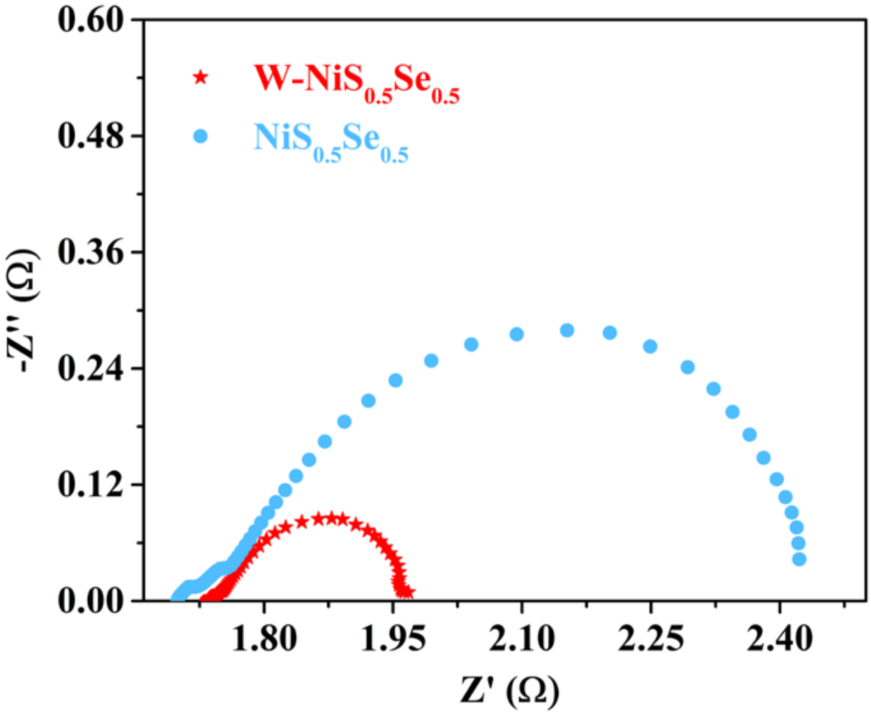

Supplementary Fig. 15 Nyquist plots of the W-$NiS_{0.5}Se_{0.5}$ and $NiS_{0.5}Se_{0.5}$ for the HER electrocatalysis.

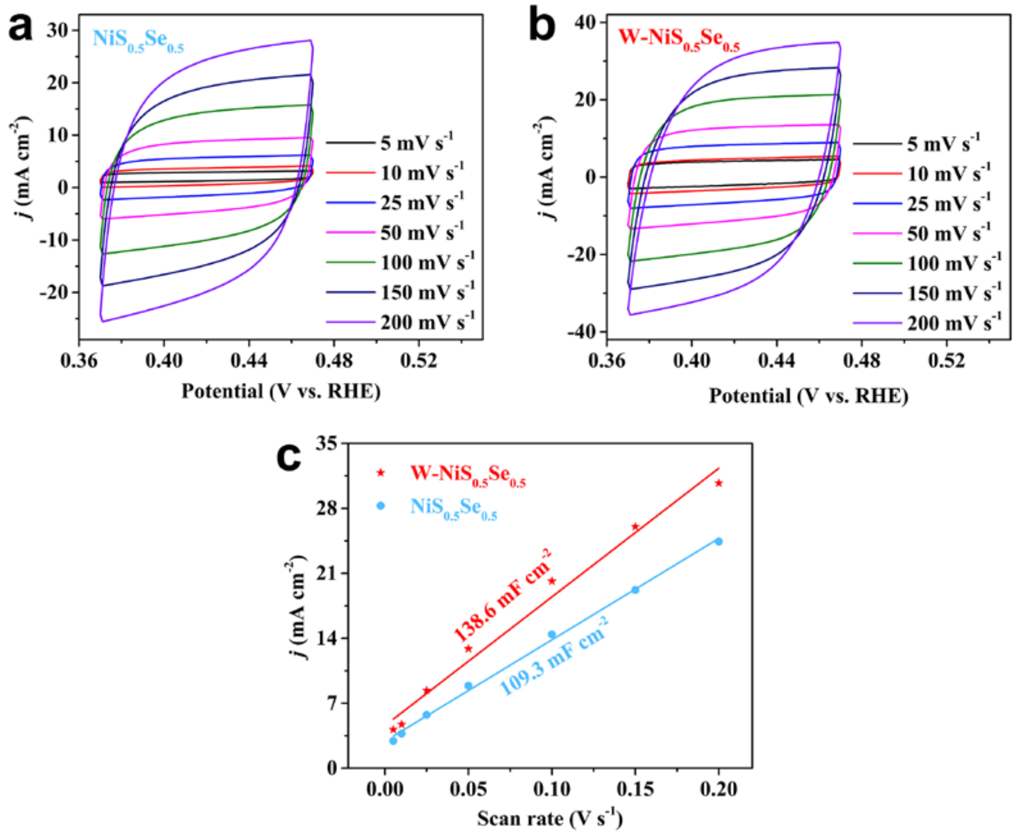

Supplementary Fig. 16 (a-b) Typical cyclic voltammograms at the scan rates ranging from 5 to 200 mV s^{-1} of the $NiS_{0.5}Se_{0.5}$ and W-$NiS_{0.5}Se_{0.5}$ with different values, the scanning potential range is from 0.37 to 0.47 V vs RHE; (b) Linear fitting of the capacitive current densities vs the scan rates.

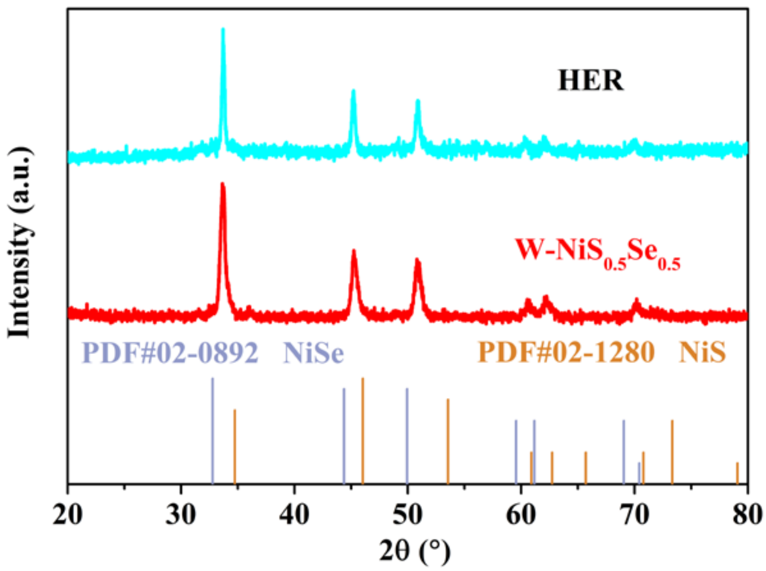

Supplementary Fig. 17 XRD characterizations of the W-$NiS_{0.5}Se_{0.5}$ after HER stability test.

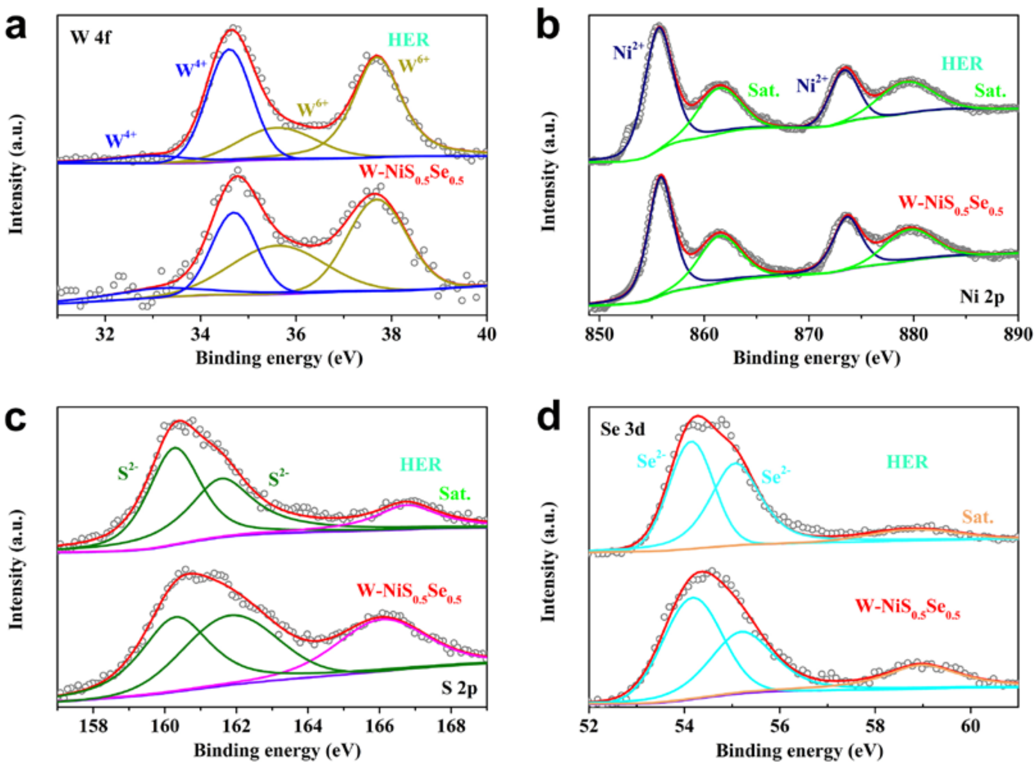

Supplementary Fig. 18 High-resolution XPS characterizations of the W-$NiS_{0.5}Se_{0.5}$ before and after HER stability test. (a) W 4f; (b) Ni 2p; (c) S 2p; and (d) Se 3d.

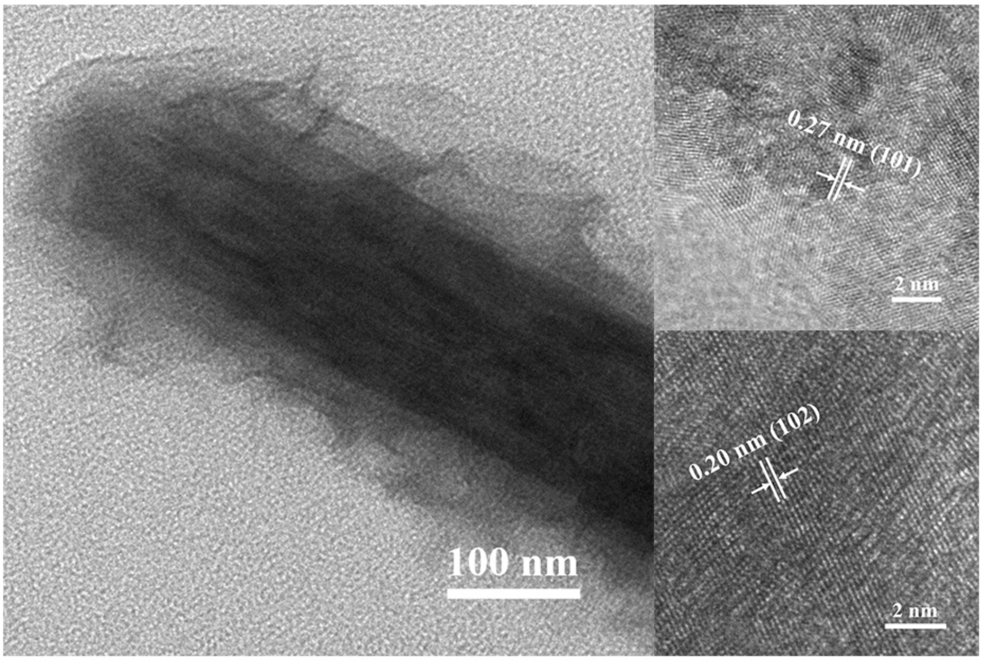

Supplementary Fig. 19 TEM and HRTEM images of the W-$NiS_{0.5}Se_{0.5}$ after HER stability test.

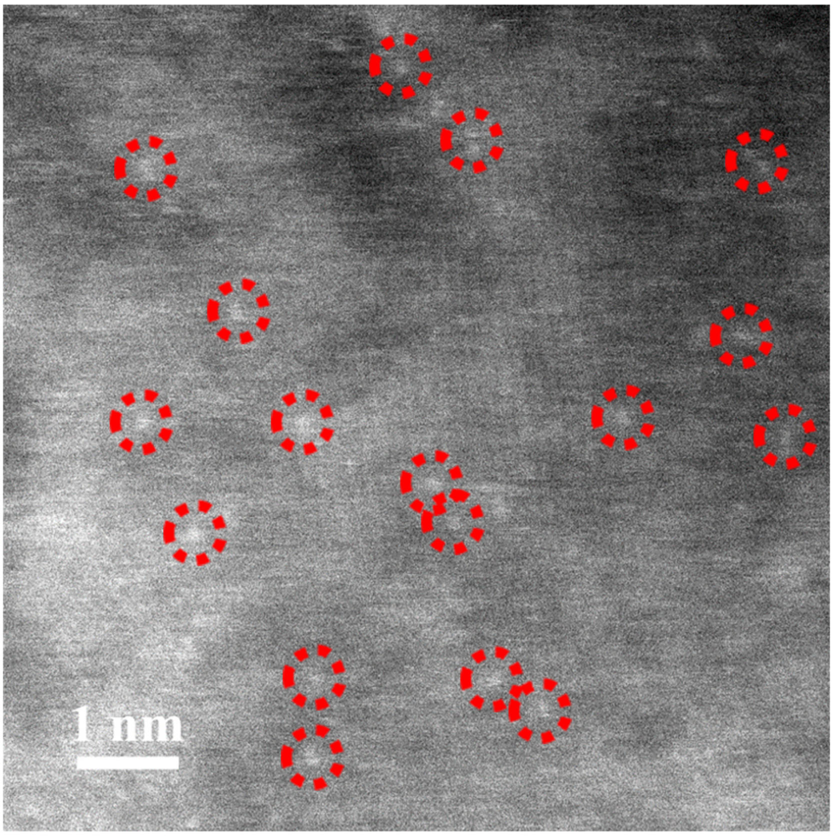

Supplementary Fig. 20 HADDF-STEM images of the W-$NiS_{0.5}Se_{0.5}$ after HER stability test.

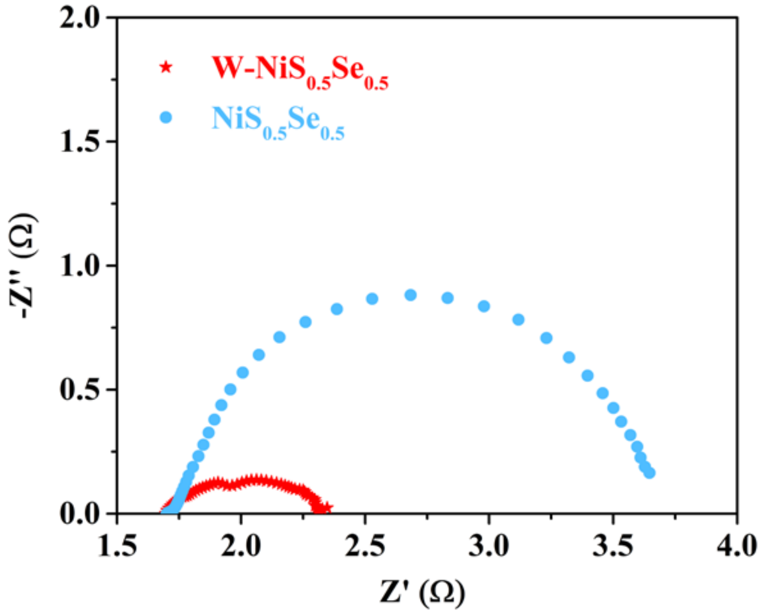

Supplementary Fig. 21 Nyquist plots of the W-$NiS_{0.5}Se_{0.5}$ and $NiS_{0.5}Se_{0.5}$ for the OER electrocatalysis.

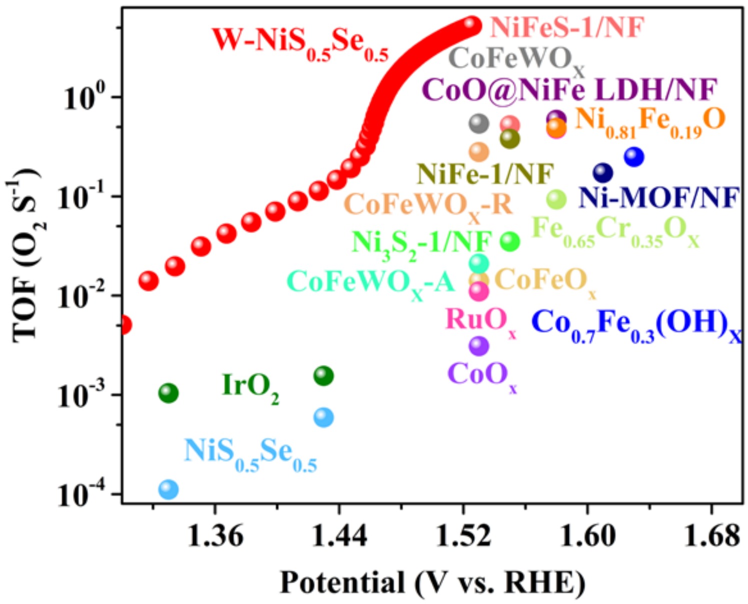

Supplementary Fig. 22 TOF value of the W-$NiS_{0.5}Se_{0.5}$ and previous reports for the OER electrocatalysis (Table S7).

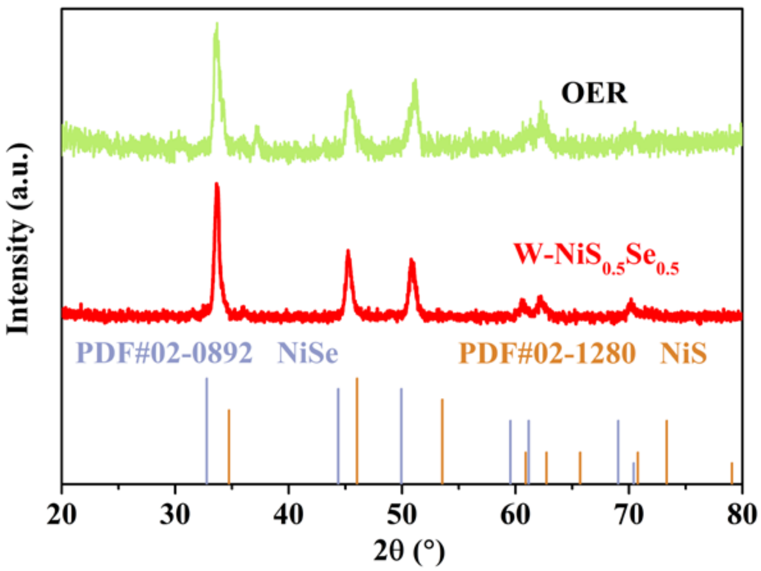

Supplementary Fig. 23 XRD characterizations of the W-$NiS_{0.5}Se_{0.5}$ after OER stability test.

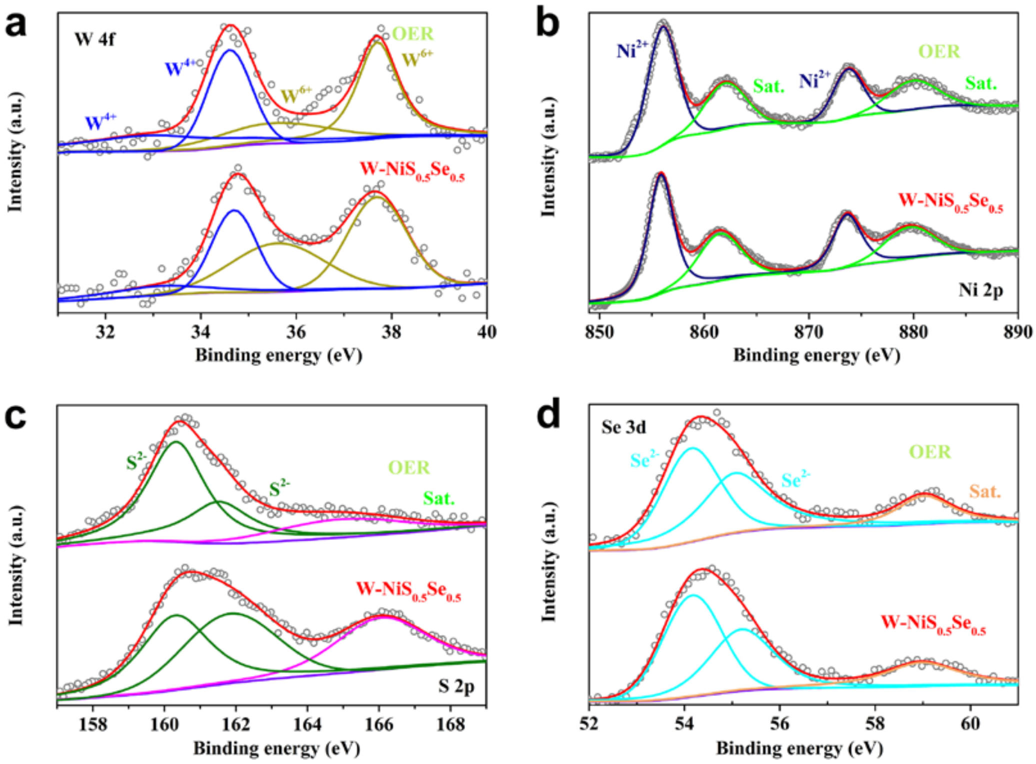

Supplementary Fig. 24 High-resolution XPS characterizations of the W-$NiS_{0.5}Se_{0.5}$ before and after OER stability test. (a) W 4f; (b) Ni 2p; (c) S 2p; and (d) Se 3d.

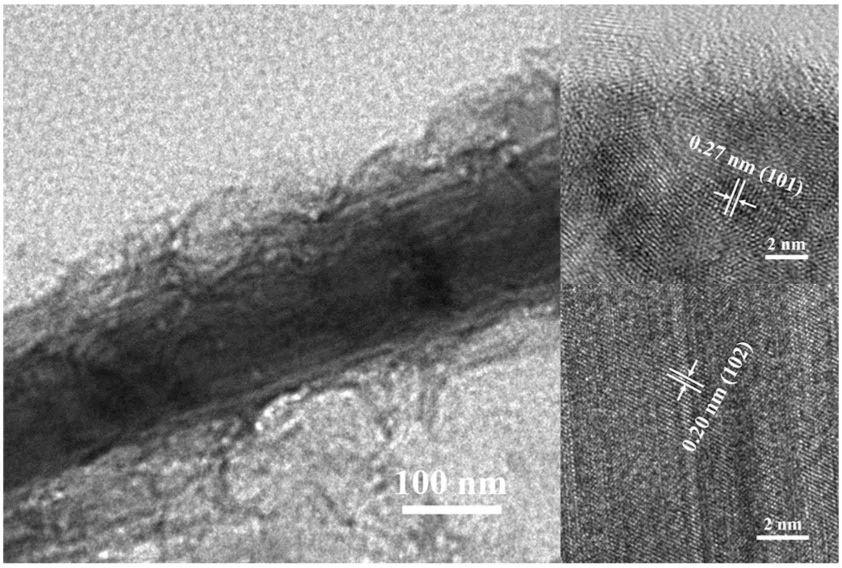

Supplementary Fig. 25 TEM and HRTEM images of the W-$NiS_{0.5}Se_{0.5}$ after OER stability test.

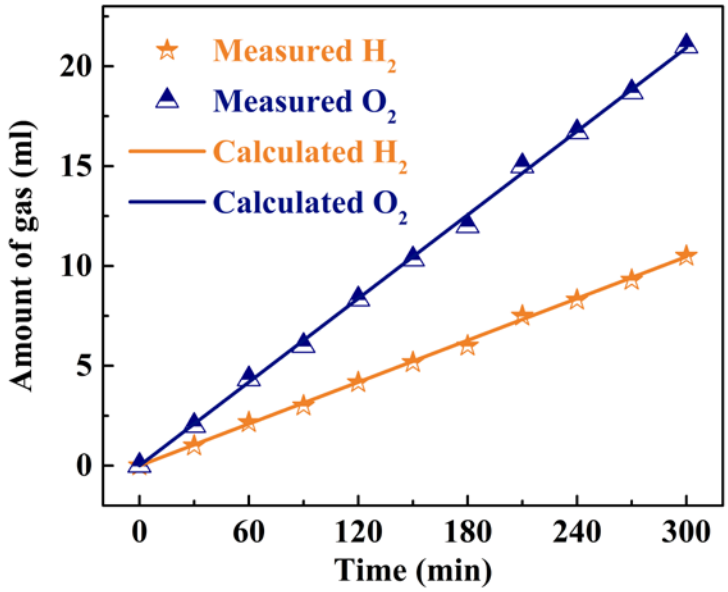

Supplementary Fig. 26 Theoretical and experimental gas volume versus time of W-$NiS_{0.5}Se_{0.5}$ for the overall water-splitting process.

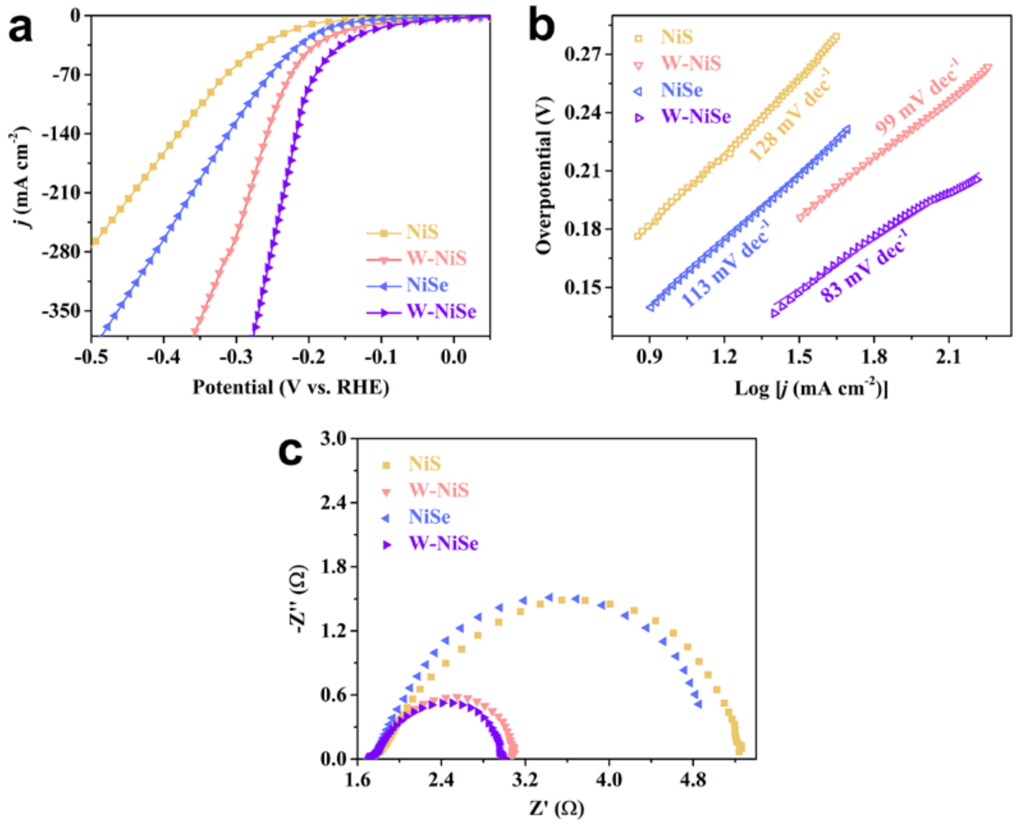

Supplementary Fig. 27 HER electrocatalytic properties of the prepared samples. (a) Polarization curves; (b) The corresponding Tafel plots derived from the polarization curves; (c) Nyquist plots of the NiS, W-NiS, NiSe and W-NiSe.

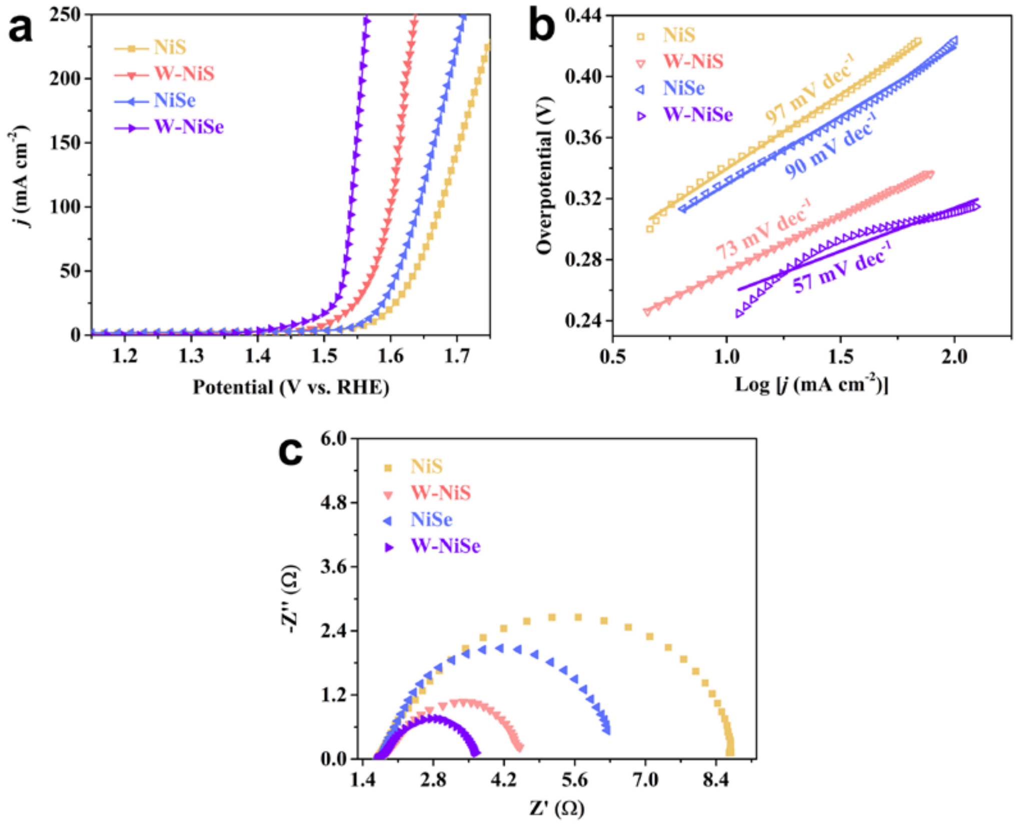

Supplementary Fig. 28 OER electrocatalytic properties of the prepared samples. (a) Polarization curves; (b) The corresponding Tafel plots derived from the polarization curves; (c) Nyquist plots of the NiS, W-NiS, NiSe and W-NiSe.

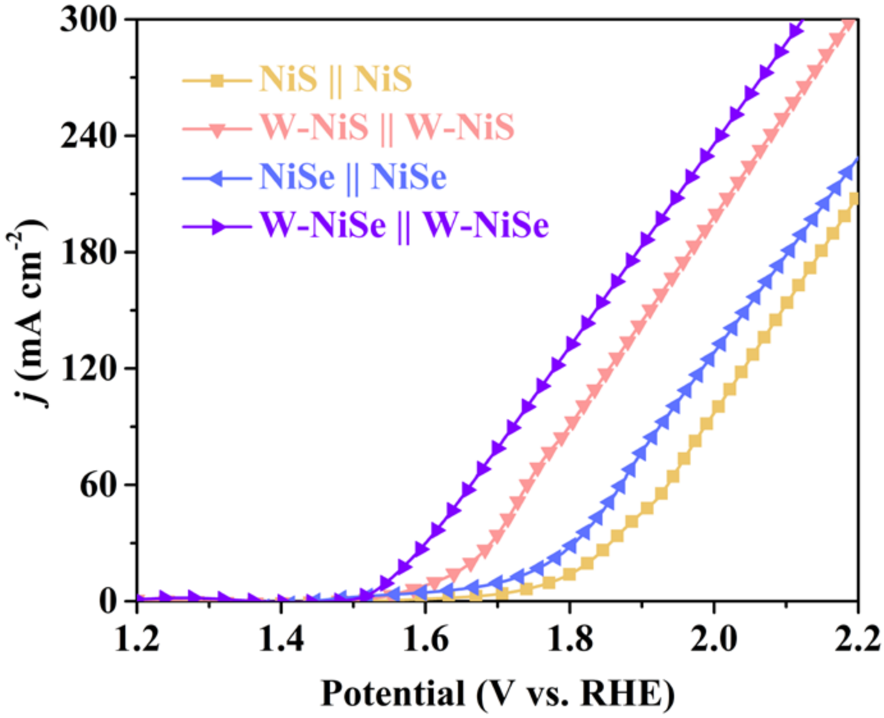

Supplementary Fig. 29 Polarization curves for the overall water splitting using the NiS, W-NiS, NiSe and W-NiSe as both the anode and cathode electrodes.

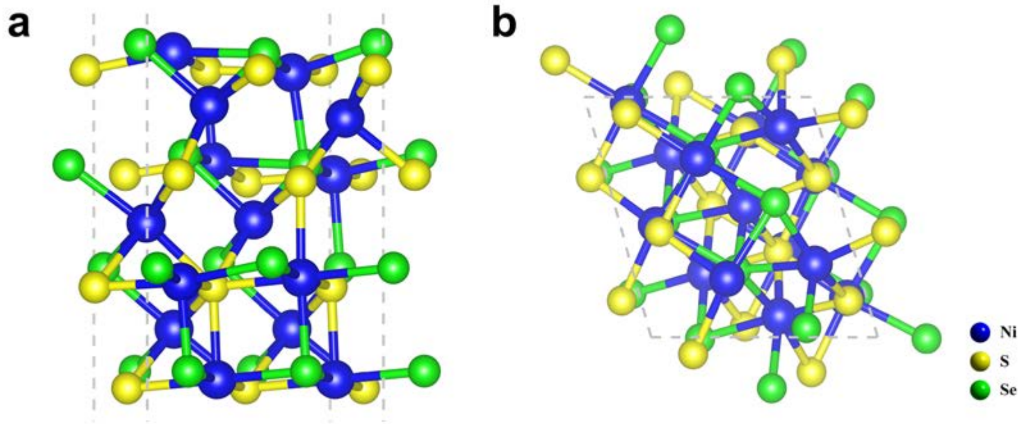

Supplementary Fig. 30 (a) The side-view schematic model of the $NiS_{0.5}Se_{0.5}$; (b) The top-view schematic model of the $NiS_{0.5}Se_{0.5}$.

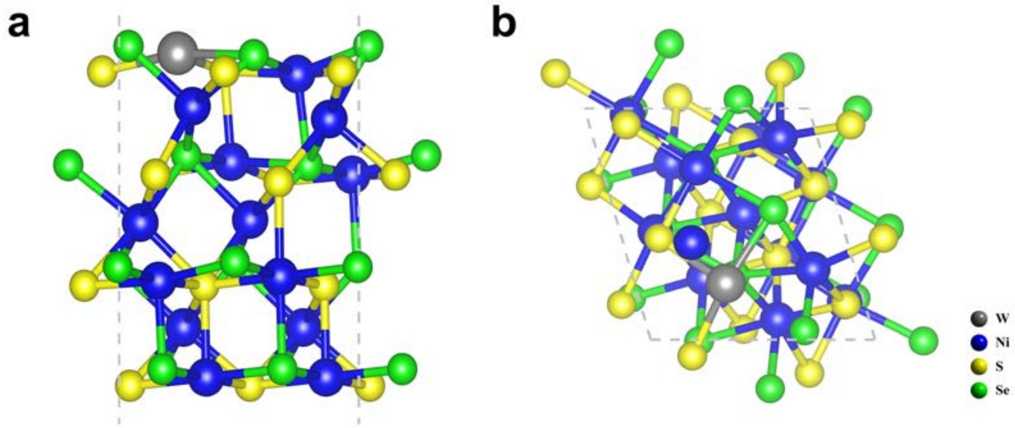

Supplementary Fig. 31 (a) The side-view schematic model of the W-$NiS_{0.5}Se_{0.5}$; (b) The top-view schematic model of the W-$NiS_{0.5}Se_{0.5}$.

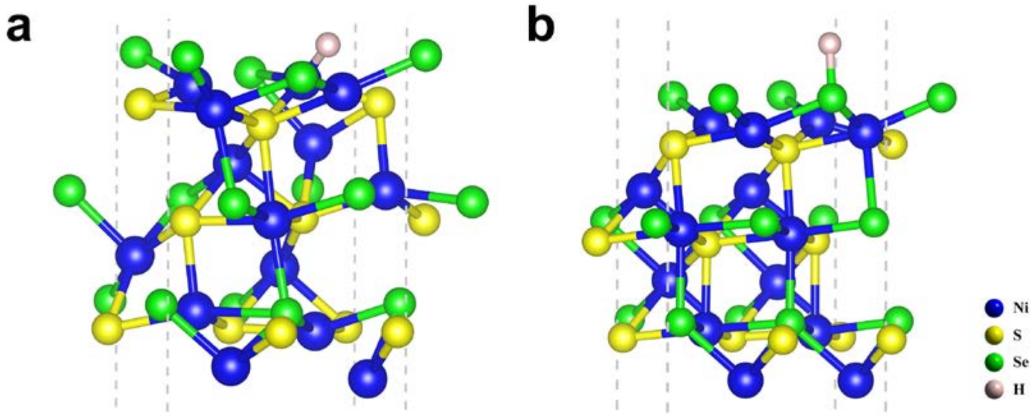

Supplementary Fig. 32 Side-view schematic model of the $NiS_{0.5}Se_{0.5}$ (Ni and Se site) with H* adsorbed on its surface.

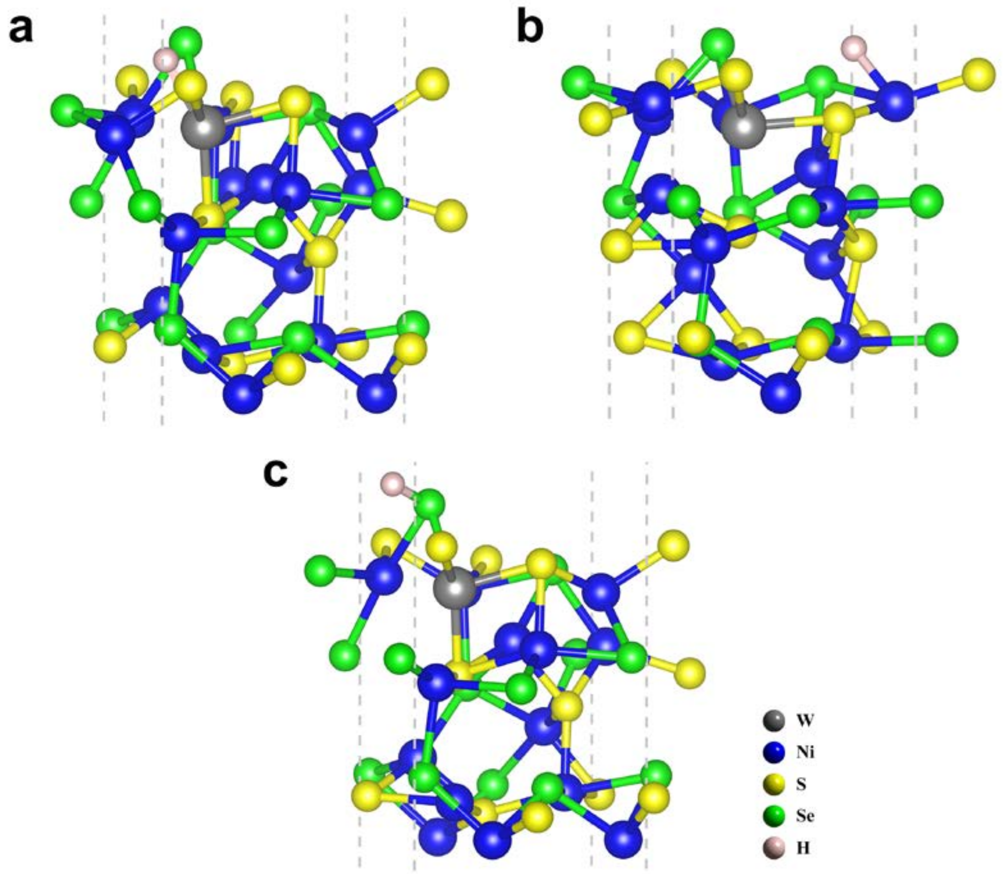

Supplementary Fig. 33 Side-view schematic model of the W-$NiS_{0.5}Se_{0.5}$ (W, Ni and Se site) with H* adsorbed on its surface.

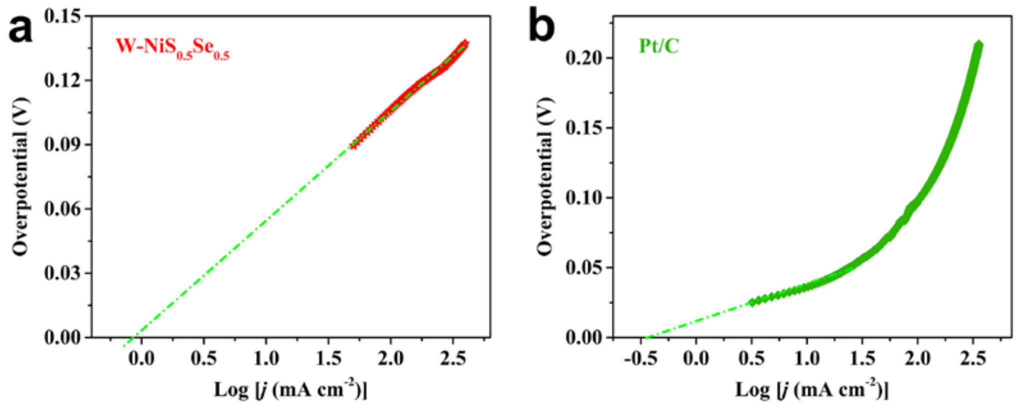

Supplementary Fig. 34 Calculation of the exchange current density, j_0, of (a) W-$NiS_{0.5}Se_{0.5}$ and (b) Pt/C catalysts by the linear fitting of Tafel plot.

The calculated j_0 of W-$NiS_{0.5}Se_{0.5}$ is 8.574×10^{-4} A cm^{-2}. The calculated j_0 of Pt/C is 3.728×10^{-4} A cm^{-2}, which agrees well with the reported data[6].

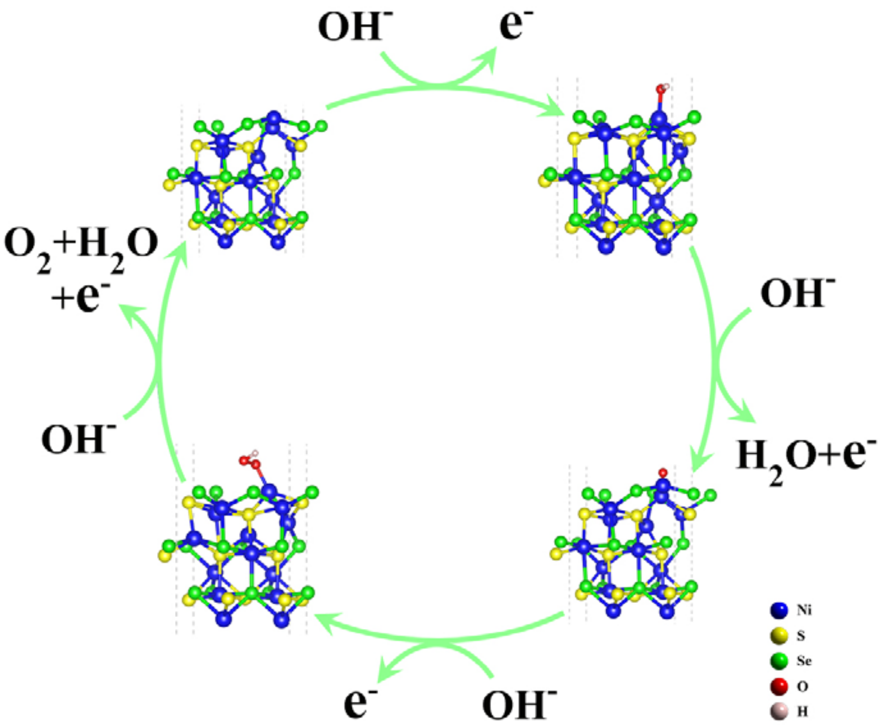

Supplementary Fig. 35 The proposed possible process of $NiS_{0.5}Se_{0.5}$ on OER process.

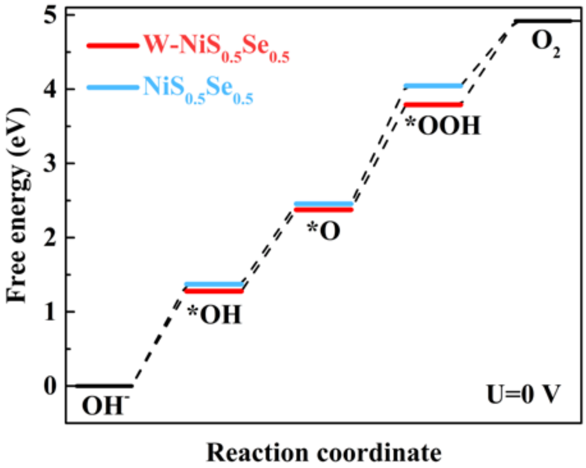

210

211 **Supplementary Fig. 36** Gibbs free-energy diagram of various oxygen species for

212 W-$NiS_{0.5}Se_{0.5}$ and $NiS_{0.5}Se_{0.5}$ during OER process at 0 V.

213

Supplementary Table 1 The atomic ratio of W: Ni: S: Se of W-$NiS_{0.5}Se_{0.5}$ at different stages of the hydrothermal process (I) 5 h; (II) 10 h; (III) 15 h; (IV) 20 h; (V) 24 h.

	W: Ni: S: Se ratio from EDX (at.%)
I	- : 54.23: 45.77: -
II	- : 52.89: 35.83: 11.28
III	- : 53.75: 23.01: 23.24
IV	- : 52.74: 24.01: 23.25
V	1.73: 49.67: 24.28: 24.32

Supplementary Table 2 The atomic ratio of W: Ni of W-$NiS_{0.5}Se_{0.5}$ samples.

	W: Ni ratio from ICP (at.%)	W: Ni ratio from EDX (at.%)	W: Ni ratio from XPS (at.%)
W-$NiS_{0.5}Se_{0.5}$	3.06: 96.94	3.37: 96.63	6.48: 93.52

Supplementary Table 3 The atomic ratio of W: Ni: S: Se of NiS, W-NiS, NiSe and W-NiSe samples.

	W: Ni: S: Se ratio from EDX (at.%)
NiS	-: 52.11: 47.89: -
W-NiS	1.51: 49.44: 49.05: -
NiSe	-: 49.93: -: 50.07
W-NiSe	1.95: 48.98: -: 48.98

Supplementary Table 4 Chemical composition and electrocatalytic performance of W-$NiS_{0.5}Se_{0.5}$, $NiS_{0.5}Se_{0.5}$, W-NiS, NiS, W-NiSe and NiSe catalysts.

Samples	W-$NiS_{0.5}Se_{0.5}$	$NiS_{0.5}Se_{0.5}$	NiS	W-NiS	NiSe	W-NiSe
η_{10} HER (mV)	39	72	196	105	152	75
η_{100} HER (mV)	106	169	342	241	280	207
Tafel HER ($mV\ dec^{-1}$)	51	79	128	99	113	83
R_{ct} HER (Ω)	0.23	0.72	3.53	1.13	3.15	1.29
η_{10} OER (mV)	171	257	342	279	330	237
η_{100} OER (mV)	239	331	445	370	412	311
Tafel OER ($mV\ dec^{-1}$)	41	62	97	73	90	57
R_{ct} OER (Ω)	0.65	1.95	6.97	2.81	4.55	1.95
C_{dl} ($mF\ cm^{-2}$)	138.6	109.3	-	-	-	-
η_{10} water splitting (V)	1.44	1.56	1.78	1.61	1.71	1.55
η_{100} water splitting (V)	1.55	1.74	2.01	1.82	1.94	1.74

Supplementary Table 5 Comparison of the HER performances between W-$NiS_{0.5}Se_{0.5}$ in this work and other reported electrocatalysts.

Materials	**Overpotential (mV)**	**Tafel (mV dec^{-1})**	**Current density (mA cm^{-2})**	**TOF (s^{-1}/mV)**	**Ref.**
W-$NiS_{0.5}Se_{0.5}$	**39/106/129**	**51**	**10/100/300**	1.105/200 5.316/135	**This work**
Co-NG-MW	175	80	10	0.385/100	7
Co-NG	147	82	10	1.189/200	8
$Mo_1N_1C_2$	132	90	10	1.46/150	9
Co-SAS-HOPNC	137	52	10	3.8/200	10
Ni-C-N NSs	60.9	32	10	6.67/200	11
NiFeS-1/NF	269	69	10	0.052/180	12
NiFe-1/NF	180	53	10	0.021/180	12
Ni_3S_2/NF	69	39	10	0.0067/180	12
Ni-doped graphene	50	45	10	0.8/300	13
Ru SAs@PN	41/71	38	20/50	1.67/25	14
Mo-SAC	132	68	10	0.148/50	15
Pt SAS/AG	12	29.33	10	0.325/12	16
Mo-Co_9S_8@C	98	90.3	10	0.5/98	17
Ni_5P_4 NPs	49	98	10	0.063/100	18
P-doped Mo_2C@C	47	71	10	0.02/100	19

Supplementary Table 6 The XPS peak position of W, Ni, S and Se for the $W\text{-}NiS_{0.5}Se_{0.5}$ before and after HER/OER stability.

	W: Ni ratio from EDX (at.%)
$W\text{-}NiS_{0.5}Se_{0.5}$	3.37: 96.63
HER	3.11: 96.89
OER	2.74: 97.26

Supplementary Table 7 Comparison of the OER performances between W-$NiS_{0.5}Se_{0.5}$ in this work and other reported electrocatalysts.

Materials	**Overpotential (mV)**	**Tafel (mV dec^{-1})**	**Current density (mA cm^{-2})**	**Scan rate (mV s^{-1})**	**TOF (s^{-1})**	**Ref.**
W-$NiS_{0.5}Se_{0.5}$	**171**	**41**	**10**	**5**	**0.052/150 1.85/250**	**This work**
NiO/Co_3O_4@NC	240	73	10	5	0.49/350	20
$CoFeWO_x$	231	32	10	5	0.54/300	21
$CoFeWO_x$-R	249	38	10	5	0.28/300	21
$CoFeO_x$	303	47	10	5	0.014/300	21
CoO_x	342	57	10	5	0.0031/300	21
$CoFeWO_x$-A	332	64	10	5	0.021/300	21
RuO_x	324	70	10	5	0.011/300	21
NiFeS-1/NF	230	55	10	5	0.52/320	12
NiFe-1/NF	370	74	10	5	0.38/320	12
Ni_3S_2/NF	400	97	10	5	0.035/320	12
Gd-CoB	230	42	10	5	-	22
Co-Mo-P/CoNWs	270	60	20	5	-	23
Ni-ZIF/Ni-B@nf	234	57	10	5	-	24
Ni/NiFeMoOx/NF	255	35	10	5	-	25
Ir/$Ni(OH)_2$	224	41	10	5	-	26

Supplementary Table 8 Comparison of the water splitting performances between W-$NiS_{0.5}Se_{0.5}$ in this work and other reported electrocatalysts.

Materials	Electrolyte	Potential (V)	Current density (mA cm^{-2})	Ref.
W-$NiS_{0.5}Se_{0.5}$	**1 M KOH**	**1.44**	**10**	**This work**
Ni_3S_2/NF	1 M KOH	1.577	10	27
Ni@NiO/NF	1 M KOH	1.71	10	28
CoS_x/Ni_3S_2/NF	1 M KOH	1.572	10	29
NiS/NiS_2/NF	1 M KOH	1.62	10	30
Ni−$Ni_{0.2}Mo_{0.8}N$/NF	1 M KOH	1.49	10	31
$FeCo_2S_4$/NF	1 M KOH	1.63	10	32
$NiSe_2$/NF	1 M KOH	1.64	10	33
MoS_2−Ni_3S_2	1 M KOH	1.5	10	34
NiFe-Se/C	1 M KOH	1.68	10	35
NiS, NiS_2	1 M KOH	1.58	10	36

Supplementary references:

1. Wang, Y. *et al.* Lattice-Strain Engineering of Homogeneous $NiS_{0.5}Se_{0.5}$ Core–Shell Nanostructure as a Highly Efficient and Robust Electrocatalyst for Overall Water Splitting. *Adv. Mater.* **32**, 1–10 (2020).
2. Zhou, S. *et al.* Engineering electrocatalytic activity in nanosized perovskite cobaltite through surface spin-state transition. *Nat. Commun.* **7**, 1–7 (2016).
3. Chen, S. *et al.* Delocalized Spin States in 2D Atomic Layers Realizing Enhanced Electrocatalytic Oxygen Evolution. *Adv. Mater.* **29**, 1–8 (2017).
4. Yin, J. *et al.* Atomic Arrangement in Metal-Doped NiS_2 Boosts the Hydrogen Evolution Reaction in Alkaline Media. *Angew. Chemie. Int. Ed.* **58**, 18676–18682 (2019).
5. Xiao, Y. *et al.* Bimetallic thin film NiCo-$NiCoO_2$@NC as a superior bifunctional electrocatalyst for overall water splitting in alkaline media. *J. Mater. Chem. A* **5**, 15901–15912 (2017).
6. Zheng, Y. *et al*. High electrocatalytic hydrogen evolution activity of an anomalous ruthenium catalyst. *J. Am. Chem. Soc.* **138**, 16174-16181 (2016).
7. Fei, H. *et al.* Microwave-Assisted Rapid Synthesis of Graphene-Supported Single Atomic Metals. *Adv. Mater.* **30**, 1–8 (2018).
8. Fei, H. *et al.* Atomic cobalt on nitrogen-doped graphene for hydrogen generation. *Nat. Commun.* **6**, 1–8 (2015).
9. Chen, W. *et al.* Rational Design of Single Molybdenum Atoms Anchored on N-Doped Carbon for Effective Hydrogen Evolution Reaction. *Angew. Chemie* -

Int. Ed. **56**, 16086–16090 (2017).

10. Sun, T. *et al.* Single-atomic cobalt sites embedded in hierarchically ordered porous nitrogen-doped carbon as a superior bifunctional electrocatalyst. *Proc. Natl. Acad. Sci. U. S. A.* **115**, 12692–12697 (2018).
11. Yin, J. *et al.* Ni−C−N Nanosheets as Catalyst for Hydrogen Evolution Reaction. *J. Am. Chem. Soc.* **138**, 14546-14549, (2016).
12. Ganesan, P., Sivanantham, A. & Shanmugam, S. Inexpensive electrochemical synthesis of nickel iron sulphides on nickel foam: Super active and ultra-durable electrocatalysts for alkaline electrolyte membrane water electrolysis. *J. Mater. Chem. A* **4**, 16394–16402 (2016).
13. Qiu, H. J. *et al.* Nanoporous Graphene with Single-Atom Nickel Dopants: An Efficient and Stable Catalyst for Electrochemical Hydrogen Production. *Angew. Chemie. Int. Ed.* **54**, 14031–14035 (2015).
14. Yang, J. *et al.* Efficient and Robust Hydrogen Evolution: Phosphorus Nitride Imide Nanotubes as Supports for Anchoring Single Ruthenium Sites. *Angew. Chemie. Int. Ed.* **130**, 9639–9644 (2018).
15. Chen, W. *et al.* Rational Design of Single Molybdenum Atoms Anchored on N-Doped Carbon for Effective Hydrogen Evolution Reaction. *Angew. Chemie. Int. Ed.* **56**, 16086–16090 (2017).
16. Ye, S. *et al.* Highly stable single Pt atomic sites anchored on aniline-stacked graphene for hydrogen evolution reaction. *Energy Environ. Sci.* **12**, 1000–1007 (2019).

17. Wang, L. *et al.* Atomically Dispersed Mo Supported on Metallic Co9S8 Nanoflakes as an Advanced Noble-Metal-Free Bifunctional Water Splitting Catalyst Working in Universal pH Conditions. *Adv. Energy Mater.* **10**, (2020).

18. Laursen, A. B. *et al.* Nanocrystalline Ni_5P_4: A hydrogen evolution electrocatalyst of exceptional efficiency in both alkaline and acidic media. *Energy Environ. Sci.* **8**, 1027–1034 (2015).

19. Chen, Y. Y. *et al.* Pomegranate-like N, P-Doped Mo_2C@C Nanospheres as Highly Active Electrocatalysts for Alkaline Hydrogen Evolution. *ACS Nano* **10**, 8851–8860 (2016).

20. Tahir, M. *et al.* High-Valence-State NiO/Co_3O_4 Nanoparticles on Nitrogen-Doped Carbon for Oxygen Evolution at Low Overpotential. *ACS Energy Lett.* **2**, 2177–2182 (2017).

21. Chen, J. *et al.* Octahedral Coordinated Trivalent Cobalt Enriched Multimetal Oxygen-Evolution Catalysts. *Adv. Energy Mater.* **10**, 1–11 (2020).

22. Haq, u. T., Mansour, S. A., Munir, A. & Haik, Y. Gold-Supported Gadolinium Doped CoB Amorphous Sheet: A New Benchmark Electrocatalyst for Water Oxidation with High Turnover Frequency. *Adv. Funct. Mater.* **30**, 1–11 (2020).

23. Hoa, V. H. *et al.* Molybdenum and Phosphorous Dual Doping in Cobalt Monolayer Interfacial Assembled Cobalt Nanowires for Efficient Overall Water Splitting. *Adv. Funct. Mater.* **30**, 1–12 (2020).

24. Xu, H. *et al.* Boronization-Induced Ultrathin 2D Nanosheets with Abundant Crystalline–Amorphous Phase Boundary Supported on Nickel Foam toward

Efficient Water Splitting. *Adv. Energy Mater.* **10**, (2020).

25. Li, Y. K. *et al*. Amorphous Ni–Fe–Mo Suboxides Coupled with Ni Network as Porous Nanoplate Array on Nickel Foam: A Highly Efficient and Durable Bifunctional Electrode for Overall Water Splitting. *Adv. Sci.* **7**, (2020).
26. Zhao, G. *et al*. An Ir/Ni$(OH)_2$ Heterostructured Electrocatalyst for the Oxygen Evolution Reaction: Breaking the Scaling Relation, Stabilizing Iridium(V), and Beyond. *Adv. Mater.* **32**, 1–9 (2020).
27. Zhang, J. *et al.* 3D Coral-Like Ni_3S_2 on Ni Foam as a Bifunctional Electrocatalyst for Overall Water Splitting. *ACS Appl. Mater. Interfaces* **10**, 31330–31339 (2018).
28. Shit, S. *et al.* Cobalt Sulfide/Nickel Sulfide Heterostructure Directly Grown on Nickel Foam: An Efficient and Durable Electrocatalyst for Overall Water Splitting Application. *ACS Appl. Mater. Interfaces* **10**, 27712–27722 (2018).
29. Sun, H. *et al*. Ni@NiO Nanowires on Nickel Foam Prepared via "Acid Hungry" Strategy: High Supercapacitor Performance and Robust Electrocatalysts for Water Splitting Reaction. *Small* **14**, 1–12 (2018).
30. Li, Q. *et al.* Construction of amorphous interface in an interwoven NiS/NiS_2 structure for enhanced overall water splitting. *J. Mater. Chem. A* **6**, 8233–8237 (2018).
31. Jia, J. *et al.* Nickel Molybdenum Nitride Nanorods Grown on Ni Foam as Efficient and Stable Bifunctional Electrocatalysts for Overall Water Splitting. *ACS Appl. Mater. Interfaces* **10**, 30400–30408 (2018).

32. Hu, J. *et al.* $FeCo_2S_4$ Nanosheet Arrays Supported on Ni Foam: An Efficient and Durable Bifunctional Electrocatalyst for Overall Water-Splitting. *ACS Sustain. Chem. Eng.* **6**, 11724–11733 (2018).

33. Zhang, J. *et al.* Self-Supported Porous $NiSe_2$ Nanowrinkles as Efficient Bifunctional Electrocatalysts for Overall Water Splitting. *ACS Sustain. Chem. Eng.* **6**, 2231–2239 (2018).

34. Yang, Y. Q. *et al.* MoS_2-Ni_3S_2 Heteronanorods as Efficient and Stable Bifunctional Electrocatalysts for Overall Water Splitting. *ACS Catal.* **7**, 2357–2366 (2017).

35. Xu, B. *et al.* Direct selenylation of mixed Ni/Fe metal-organic frameworks to NiFe-Se/C nanorods for overall water splitting. *J. Power Sources* **366**, 193–199 (2017).

36. Luo, P. *et al.* Targeted synthesis of unique nickel sulfide (NiS, NiS_2) microarchitectures and the applications for the enhanced water splitting system. *ACS Appl. Mater. Interfaces* **9**, 2500–2508 (2017).